



CHORUS

This is the accepted manuscript made available via CHORUS. The article has been published as:

Long-range and local crystal structures of the $\text{Sr}_{1-x}\text{Ca}_x\text{RuO}_3$ perovskites

Loi T. Nguyen, Milinda Abeykoon, Jing Tao, Saul Lapidus, and R. J. Cava

Phys. Rev. Materials **4**, 034407 — Published 20 March 2020

DOI: [10.1103/PhysRevMaterials.4.034407](https://doi.org/10.1103/PhysRevMaterials.4.034407)

Long-range and local crystal structures of the $\text{Sr}_{1-x}\text{Ca}_x\text{RuO}_3$ Perovskites

Loi T. Nguyen¹, Milinda Abeykoon², Jing Tao³, Saul Lapidus⁴, and R.J. Cava¹

¹Department of Chemistry, Princeton University, Princeton, New Jersey 08544, USA

²National Synchrotron Light Source II, Brookhaven National Laboratory, Upton, New York
11973, USA

³Condensed Matter Physics & Materials Science Division, Brookhaven National Laboratory,
Upton, NY 11973, USA

⁴X-ray Science Division, Advanced Photon Source, Argonne National Laboratory, Lemont, Illinois
60439, USA

Abstract

The crystal structures of the $\text{Sr}_{1-x}\text{Ca}_x\text{RuO}_3$ ($0 \leq x \leq 1$) perovskites are investigated using both long range and local structural probes. High resolution synchrotron powder X-ray diffraction characterization at ambient temperature shows that the materials have orthorhombic long range crystal structures to high precision, and we support previous work showing that Ca^{2+} substitution for Sr^{2+} primarily changes the tilting of rigid corner-sharing RuO_6 octahedra at their shared oxygen vertices. X-ray pair distribution function analysis for SrRuO_3 , CaRuO_3 and one intermediate composition show them to display monoclinic symmetry at the local level; when averaged over different domain orientations this yields orthorhombic symmetry on the long range, and no long range or local phase transitions are observed between 80 and 300 K for materials with intermediate compositions. High-resolution transmission electron microscopy shows that the Sr/Ca distribution is random at the nanoscale. We plot magnetic characteristics such as the ferromagnetic T_c , Curie-Weiss theta, effective moment, and ambient temperature susceptibility vs. the octahedral tilt and unit cell volume.

Keywords: perovskites, ruthenates, synchrotron diffraction, x-ray PDF, electron microscopy.

Introduction

The ruthenate perovskites, while of long interest, have attracted increased attention since the single layer material Sr_2RuO_4 was found to superconduct at 1.5 K [1]. This family is widely viewed as being an ideal system for investigating correlated materials[2],[3],[4],[5],[6],[7], with behavior that ranges from ferromagnetic SrRuO_3 to paramagnetic CaRuO_3 to superconducting Sr_2RuO_4 . Calculations of the magnetic properties of SrRuO_3 and CaRuO_3 argue that the magnetism is governed by the electronic band structure and correlation between Hubbard and Hund's interactions[8],[9]. There are many studies on ferromagnetic SrRuO_3 in bulk and thin film form (see, e.g. [10],[11],[12],[13],[14]).

For the $\text{Sr}_{1-x}\text{Ca}_x\text{RuO}_3$ perovskites, the reported orthorhombic symmetry unit cells are larger in volume than simple cubic perovskite cells due to the tilts of the RuO_6 octahedra at their shared vertices. (a and c are square root of 2 larger than a simple cubic perovskite cell while b is double the simple cubic perovskite cell value). Although Ca and Sr are both divalent and thus the electron content of the system is unchanged in $\text{Sr}_{1-x}\text{Ca}_x\text{RuO}_3$, the difference in the resulting tilt angles between the rigid RuO_6 octahedra due to the accommodation of different size Sr and Ca ions in the perovskite cavities is widely believed to be the structural feature that distinguishes ferromagnetic SrRuO_3 from paramagnetic CaRuO_3 [15],[16],[17],[18]. Density Functional Theory calculations argue that the larger orthorhombic distortion for CaRuO_3 compared to SrRuO_3 suppresses the ferromagnetism[19],[20],[21],[22],[23] and CaRuO_3 is claimed to be at a critical point between ferromagnetic and paramagnetic states [24],[25],[26]. Many experimental studies of the $\text{Sr}_{1-x}\text{Ca}_x\text{RuO}_3$ perovskite system have been reported [27],[28],[29],[30],[31],[32],[33].

Here we present a high resolution synchrotron powder diffraction study of the long range crystal structures in the $\text{Sr}_{1-x}\text{Ca}_x\text{RuO}_3$ perovskite solid solution, a study of the local crystal structures by X-ray pair distribution function (PDF) analysis, and high resolution transmission electron microscopy (HRTEM) and scanning transmission electron microscopy (STEM) studies of selected members of the series, accompanied by the magnetic characterization of the materials. The synchrotron diffraction study allows us to determine that the ambient temperature long range crystal structures are orthorhombic to high precision, and the PDF studies show that the materials are locally (at the 2-5 Angstrom scale) monoclinically distorted. No structural phase transitions are observed for selected materials down to 80 K. The electron microscopy

studies show that the solid solution is highly chemically homogeneous. The magnetic properties of the solid solution materials show highly systematic behavior and coupled with the structural characterization allow for a correlation of the fundamental magnetic and structural characteristics of the system with the crystal structures. All of the basic magnetic properties appear to scale simply with the perovskite tilt angles and the unit cell volume.

Experiment

High quality single-phase powder samples of $\text{Sr}_{1-x}\text{Ca}_x\text{RuO}_3$ ($0 \leq x \leq 1$) were synthesized by a solid-state method, using SrCO_3 , CaCO_3 and RuO_2 (Alfa Aesar > 99.95%) as starting materials. SrCO_3 and CaCO_3 were dried in an oven at 120°C for 3 days before use. Stoichiometric ratios of the starting materials were mixed thoroughly in a mortar and pestle, transferred to alumina crucibles and heated in air at 1000°C for 24 hours. The powders were reground and heated in air at 1100°C , 1200°C , 1300°C and 1400°C for 12 hours at each temperature. The phase purities were initially determined through laboratory powder X-ray diffraction using a Bruker D8 Advance Eco with $\text{Cu K}\alpha$ radiation and a LynxEye-XE detector. Single-phase powder samples of the $\text{Sr}_{1-x}\text{Ca}_x\text{RuO}_3$ perovskites were then loaded into Kapton sample capillary tubes and synchrotron powder x-ray diffraction characterization was performed at beamline 11-BM at Argonne National Laboratory. The structural refinements were performed with GSAS [34]. The crystal structure drawings were created by using VESTA [35].

Electron diffraction experiments were performed at Brookhaven National Laboratory using a double-Cs corrected JEOL ARM 200F transmission electron microscope (TEM; JEOL, Tokyo, Japan) equipped with multiple sample holders including a double-tilt holder and a Gatan liquid nitrogen sample cooling holder. TEM samples of $\text{Sr}_{1-x}\text{Ca}_x\text{RuO}_3$ ($x = 0, 0.3, 0.5$ and 1) were prepared directly from the powder material by grinding. Energy dispersive X-ray spectroscopy (EDX) was performed to examine the elemental distributions in different particles.

The X-ray PDF measurements were carried out at beamline 28-ID-1 at NSLS-II, at Brookhaven National Laboratory. The X-ray PDF data on 11 samples in the $\text{Sr}_{1-x}\text{Ca}_x\text{RuO}_3$ solid solution system were collected at room temperature with a 75 keV beam energy and analyzed by using the program PDFgui [36]. Scattering data were normalized to 0.5 second/frame. Temperature-dependent PDF studies for several samples were obtained on the same experimental apparatus.

The magnetic susceptibilities of $\text{Sr}_{1-x}\text{Ca}_x\text{RuO}_3$ powders were measured in a Quantum Design Dynacool PPMS equipped with a VSM option. The magnetic susceptibilities between 1.8 and 300 K, defined as M/H , where M is the sample magnetization and H is the applied field, were measured at the field of $H = 1$ kOe.

Results

The Long-range crystal structure

The high signal to noise ratio and high precision of the synchrotron diffraction measurements allow us to determine that all the perovskite samples were single phase within an estimated 1 part in 10^3 and that all the materials in the $\text{Sr}_{1-x}\text{Ca}_x\text{RuO}_3$ solid solution are orthorhombic to high precision at ambient temperature. All materials crystallize in the orthorhombic space group $Pnma$ (No. 62), consistent with previous work [28],[37]. As examples of the changes in the diffraction patterns observed in the solid solution, **Figure S1** [51] shows the shifts of the (200), (121) and (002) peaks as the lattice parameters change from SrRuO_3 to CaRuO_3 . Rietveld refinements of the CaRuO_3 , SrRuO_3 and $\text{Sr}_{0.7}\text{Ca}_{0.3}\text{RuO}_3$ samples are shown as examples in **Figure S2** [51]. Excellent fits are found to the $Pnma$ orthorhombic perovskite structural model of the GdFeO_3 -type structure type, a perovskite with an a^+b^- type tilt system [38]. The insets show a blow-up of the high angle diffraction region, and in specific show the quality of the orthorhombic structure fit at high angles. The lattice parameters, bond angles and bond lengths are listed in **Table 1** for all studied members of the solid solution series.

As shown in **Figure 1**, which plots the pseudo-cubic perovskite subcell values for a , b and c (orthorhombic a and c divided by the square root of 2, orthorhombic b divided by 2), while both b and c lattice parameters decrease monotonically as the Ca content in the $\text{Sr}_{1-x}\text{Ca}_x\text{RuO}_3$ perovskite solid solution increases, the lattice parameter a does not vary much in comparison and displays a minimum value near $x = 0.4$. Near this composition the material is dimensionally nearly cubic. This general behavior is consistent with one earlier report [32], although a different study [30] reported a slightly different trend of lattice parameters for samples synthesized at 1000°C . (In our hands, a synthetic temperature 1000°C is too low to obtain pure phases; significantly higher temperatures are required.) Based on the structural refinements of the atomic positions against the synchrotron diffraction data, the Ru-O bond lengths do not change significantly within the scatter (**Figure S3d**) [51], and neither do the O-Ru-O bond angles - the angles that describe the shape of the corner-sharing RuO_6 octahedra, as shown in **Figure S3c**

[51]. The slope of the variation of average (Sr/Ca)-O bond length with composition changes subtly between $x = 0.3$ and $x = 0.4$, shown in **Figure S3b** [51].

The effective coordination number of M^{2+} ($M = \text{Ca/Sr}$) decreases on going from SrRuO_3 to CaRuO_3 . The decrease in effective coordination number, while it depends on what appears to be an arbitrary definition of bonding vs. non-bonding interactions in A-O perovskites, reflects the commonly accepted view that Ca^{2+} ion typically takes fewer near oxygen neighbors than the larger Sr^{2+} ion. According to the ICSD database, the most common Ca-O bond lengths range from 2.3 to 2.7 Å, and the Sr-O bond lengths range from 2.5 to 2.9 Å. The coordination numbers may therefore be considered as 9 for both CaRuO_3 and SrRuO_3 if one allows for distances within 2 sigma of the mean. However, there is one very long Ca-O distance (3.14 Å) in CaRuO_3 among these, which is not reasonable. Therefore, when this long distance is excluded, Ca is 8-coordinated to oxygen in CaRuO_3 .

This is illustrated in **Figure S4** [51], which also includes the equivalent views for the well-known perovskites SrTiO_3 and CaTiO_3 . (The ideal cubic perovskite cavity has 12 equidistant oxygens in a cuboctahedron geometry for an A atom sitting in the center of the perovskite cavity, as is seen for example for SrTiO_3 at 300 K.) We note that at equivalent cavity volumes, **Figure S4** [51] shows that the ruthenate perovskites are more distorted than the titanate perovskites. The increasing off-center position of the A site ions can be represented by plotting the variance in A-O bond lengths $(\sum((A-O)_i^2 - (A-O)_{\text{avg}}^2)/(n-1))$ for $n = 12$ as a function of x (**Figure S5**) [51]; the variance increases significantly when going from SrRuO_3 to CaRuO_3 . A subtle crossover point exists where the A atoms on average move to slightly different positions within the perovskite cavity (**Figure S3b**) [51]. Both the cell volume per formula unit and the cavity volume are a smooth function of x (**Figures 2a and 2b**), however. Finally, although it is widely understood that the “shrinkage” of perovskites in which the size of the A site ion decreases in radius is primarily due to the rigid twisting of the octahedra, this can be shown clearly in the current case through a plot of the fraction of cavity volume, i.e. (total cavity volume of the cell)/(total cell volume), as a function of x , (**Figure 2c**) which is very nearly a constant between (84.5 and 85%), though increasing slightly with increasing Ca content (x). This is a good indication that the RuO_6 octahedra are essentially rigid in this case, while also reflecting that the A site cavity in perovskites occupies a relatively large part of the total cell volume.

When preparing to connect the magnetic properties to the structural properties, we must first determine how the Ru-O network deviates from the ideal cubic perovskite crystal structure with composition in the solid solution. **Figure 3** thus shows the composition dependence of the perovskite tilt angles - the measure of distortion that the Ru-O-Ru angle deviates from the ideal value of 180 degrees where the BX_6 framework gets distorted. Since the Ru-O-Ru bond angle decreases from 163° in $SrRuO_3$ to 150° in $CaRuO_3$, the hybridization (electron-electron interaction between 2 Ru-ions through the oxygen bridge) is stronger in $SrRuO_3$ than $CaRuO_3$.

Plots for the high symmetry [001], [110] and [111] directions [39] in the $Sr_{1-x}Ca_xRuO_3$ solid solution are shown. ([001] tilt = $\tan^{-1} \left\{ \left[4(u_{x(2)}^2 + v_{x(2)}^2)^{\frac{1}{2}} \right] / (a^2 + b^2)^{\frac{1}{2}} \right\}$, [110] tilt = $\theta = \text{average of } \tan^{-1} \left\{ [4\sqrt{2}w_{x(2)}] / (a^2 + b^2)^{\frac{1}{2}} \right\}$ and $\tan^{-1} \left\{ [4(u_{x(1)}^2 + v_{x(1)}^2)^{\frac{1}{2}}] / c \right\}$, and [111] tilt = $\psi = \cos^{-1}(\cos \theta \times \cos \phi)$, where $u_{x(1)}$, $u_{x(2)}$, $v_{x(1)}$, $v_{x(2)}$ and $w_{x(2)}$ are atomic displacements from the ideal positions; and a , b and c are lattice parameters). From $SrRuO_3$ to $CaRuO_3$, all three tilt angles increase with composition, quantifying how the RuO_6 framework is more distorted in $CaRuO_3$ than in $SrRuO_3$. The tilt angles plotted have been determined from the internal atomic coordinates [39]. Also in **Figure 4a** plotted are a single parameter characterizing the average tilt of the octahedra (taken as the average of the tilt values over the [001] [110] and [111] directions) as a function of both the theoretical (Goldschmidt) and actual observed perovskite tolerance factors [40],[41]. (Tolerance factor $\tau = \langle A - O \rangle / (\sqrt{2} \langle B - O \rangle)$, using the theoretical ionic radii taken from the Shannon table [41]). The variance of the A-O (A=Sr/Ca) bond lengths as a function of the average tilt in $Sr_{1-x}Ca_xRuO_3$ perovskites is also plotted in **Figure 4b**. We note that the tolerance factor is a commonly used single parameter to describe the potential for distortion from cubic symmetry in perovskites. When the tolerance factor is close to the value of 1, perovskite structures become cubic. For lower values they are typically orthorhombic [39],[40]. Our analysis allows for a more detailed quantification of the real distortions for the current case; detailed studies of other perovskites are also of interest.

The Local crystal structure

The X-ray PDF refinements for the $Sr_{1-x}Ca_xRuO_3$ perovskites with $x = 0, 0.3$ and 1 are seen in **Figure S6** [51]. ($G(r) = \frac{2}{\pi} \int_{Q_{min}}^{Q_{max}} Q[S(Q) - 1] \sin QrdQ$, where $G(r)$ is the probability of finding a pair of atoms separated by a distance of r ; Q is the magnitude of the scattering vector

and $Q = 4\pi \sin \theta/\lambda$, and $S(Q)$ is the structural function which is the properly corrected and normalized powder diffraction intensity measured from Q_{\min} to Q_{\max}). The local structures are taken as being represented by atomic separations that are less than 5 Å, whereas the average structures are represented by larger separations. For both CaRuO_3 and SrRuO_3 , there are three relatively sharp peaks between 2.3-2.9 Å, corresponding to the presence of three different local M^{2+} -O bond lengths (M = Ca or Sr) for the ions in the perovskite cavities. In $\text{Sr}_{0.7}\text{Ca}_{0.3}\text{RuO}_3$, the smearing of the features in this range implies that the local Sr and Ca positions in the perovskite cavities are impacted by the positions of Ca and Sr in the neighboring cavities [31],[32]. As seen in **Figure 5**, the long range structures determined by synchrotron powder X-ray diffraction refinements of CaRuO_3 and SrRuO_3 agree well with the long-range structures determined by the X-ray PDF data. The local structures show some deviations, however, shown in **Figure 6**, where lower symmetry monoclinic models fit better than the orthorhombic structural models for distances below 5 Å. These monoclinic structures arise from very small short range distortions (**Table 2**) that are averaged over different monoclinic domain orientations to yield the orthorhombic long range structures. The cell volumes are less than 0.5% different, such that in the orthorhombic structure they are 227.12 Å³ for CaRuO_3 and 241.95 Å³ for SrRuO_3 . In the monoclinic structures, these values are 227.51 Å³ and 242.79 Å³, respectively. Finally, the temperature dependent X-ray PDF patterns for $\text{Sr}_{0.7}\text{Ca}_{0.3}\text{RuO}_3$ and $\text{Sr}_{0.6}\text{Ca}_{0.4}\text{RuO}_3$, shown in **Figure S7** [51], reveal no evidence for either local or long-range structural phase transitions between 80 and 300 K. Sharper peaks are observed at 80 K, consistent with expectations for decreasing atomic thermal vibrations with decreasing temperature [42],[43].

Figure 7a shows the ED, EDX, HRTEM and atomic-resolution high-angle annular dark-field (HAADF) STEM (the image intensity is sensitive to the atomic numbers of the elements in this technique) data for $\text{Sr}_{0.7}\text{Ca}_{0.3}\text{RuO}_3$ in the [010] zone (i.e. looking down the crystallographic *b* axis) at ambient temperature, obtained from an area of 150 nm in diameter. The ED data shows bright sharp spots with a uniform spacing of approximately 0.28 nm. EDX, HRTEM and HAADF-STEM confirm that $\text{Sr}_{0.7}\text{Ca}_{0.3}\text{RuO}_3$ is very structurally and chemically homogeneous. In-situ cooling experiments were performed on $\text{Sr}_{0.7}\text{Ca}_{0.3}\text{RuO}_3$ and no structural phase transition was observed in the ED patterns obtained at 90 K (not shown). This is opposite to the case seen in the $\text{La}_{0.23}\text{Ca}_{0.77}\text{MnO}_3$ manganite, for example, which has a dynamic competition between charge-ordered and charge-disordered phases that causes structural phase separation [44].

Similar measurements on a $\text{Sr}_{0.5}\text{Ca}_{0.5}\text{RuO}_3$ sample are also presented in **Figure 7b**. The presence of relatively large structural defects can be seen in the HRTEM image from $\text{Sr}_{0.5}\text{Ca}_{0.5}\text{RuO}_3$, while the areas between the defects remain structurally and chemically homogeneous as shown in the HAADF-STEM image.

Magnetic properties

Figure 8a shows the magnetic susceptibility for the $\text{Sr}_{1-x}\text{Ca}_x\text{RuO}_3$ perovskites as function of temperature from 1.8 to 300 K - the inverse susceptibility (minus the temperature independent contribution to the susceptibility) is shown in panel **8b**. The latter panel shows clearly that at high temperature, the magnetic susceptibility follows the Curie-Weiss law, with the slopes of the lines, which are due to the value of the magnetic moment, displaying little variation with temperature. The difference between susceptibility at 300 K and the temperature independent susceptibility (**Table S1**) [51] decreases systematically as the Ca content in the perovskite increases as shown in **Figure 9a**, i.e. the material becomes less magnetic with increasing Ca content. The susceptibility at 300 K is a sum of a temperature independent paramagnetic term, a relatively small contribution, which presumably arises from the presence of non-magnetic electrons in broad electronic bands, and a temperature dependent term, which arises from the electrons that give rise to the magnetism. The temperature-independent term is essentially independent of composition, although oscillating slightly and previously observed in a similar system in [45], and the susceptibility is dominated by the magnetic electrons, even at temperatures as high as 300 K for CaRuO_3 .

The fitting ($\chi = C/(T - \theta_{\text{CW}}) + \chi_0$ (where C is the Curie constant, T is temperature, θ_{CW} is the Curie Weiss temperature and χ_0 is the temperature-independent contribution) to the data shown in **Figure 8b** yields the effective moment ($\mu_{\text{eff}} = \sqrt{8C}$) and Curie-Weiss temperature as a function of Ca content, plotted in **Figures 9b-c**. The results indicate a linearly decreasing Curie-Weiss temperature when the Ca content in the $\text{Sr}_{1-x}\text{Ca}_x\text{RuO}_3$ solid solution increases, consistent with many previous studies [30],[31],[32],[46],[47],[48],[49]. The sign of the Curie-Weiss theta changes from positive to negative between $x=0.5$ and 0.6 , nominally reflecting the shift from dominantly ferromagnetic to dominantly antiferromagnetic interactions in the solid solution. Also, the fits show that the effective magnetic moment per mole increases slightly on going from SrRuO_3 to CaRuO_3 . Comparison to the magnetic data presented in other studies shows that while our data are highly systematic, previous data are not universally so [29], [30].

Magnetism-structure correlations

The magnetism-structure correlations found in the current study are summarized in **Figures 8-10**. The monotonic variation of magnetic properties with the Ca content in the solid solution is clear, with the figures showing that this variation can be attributed to differences in the octahedral tilts, which change with Ca content and are clearly defined by our structural study. Significantly, the dramatic decrease of the Curie-Weiss theta with Ca content in the $\text{Sr}_{1-x}\text{Ca}_x\text{RuO}_3$ solid solution (**Figure 9c**), and the accompanying decrease in ferromagnetic T_c show a simple variation with both the octahedral tilt and the unit cell volume (**Figure 10**); within error, for both types of correlation, nicely linear behavior is observed. The ferromagnetic T_c of SrRuO_3 when compressed by applied pressure decreases with unit cell volume via a different trend when compared to the substitution of Ca in $\text{Sr}_{1-x}\text{Ca}_x\text{RuO}_3$ [50]; T_c is significantly higher at any given cell volume. This implies that the magnetic transition from ferromagnetic SrRuO_3 to antiferromagnetic CaRuO_3 in the $\text{Sr}_{1-x}\text{Ca}_x\text{RuO}_3$ solid solution is due not only to a decrease in the cell volume (and the accompanying octahedral tilt), but is also strongly influenced by other factors, such as the Sr-Ca mixing and the electronegativity differences between Ca and Sr.

Conclusion

The average crystal structure of the $\text{Sr}_{1-x}\text{Ca}_x\text{RuO}_3$ solid solution, studied by synchrotron x-ray diffraction, is determined to be orthorhombic to high precision, supporting earlier studies. The local structure studied by the X-ray PDF method confirms that the average structure is a good description of the materials at longer distances. At shorter distances both SrRuO_3 and CaRuO_3 appear to be locally monoclinic. The local distortions, which are seen at the shorter than 5 angstrom length scale, are averaged over different orientations to yield the longer range orthorhombic structures. In SrRuO_3 , the Ru-O-Ru angles in the perovskite matrix formed by the corner-sharing RuO_6 octahedra are closer to linear than the ones in CaRuO_3 but nonetheless deviate significantly from an ideal 180 degree angle present in cubic perovskites. Thus our data support many previous studies showing that both SrRuO_3 and CaRuO_3 are not cubic perovskites, with the octahedral tilts being significantly larger in the latter material than the former material. The peculiarities of the octahedral tilting in the solid solution make the material look nearly cubic in a small range of Ca contents near $x=0.4$, but this is an artifact because tilts remain present in the octahedral network. The fundamental magnetic characteristics of the system scale linearly with both the octahedral tilt angles and the unit cell volume. We imagine that either case

is consistent with electronic structure calculations and previous models for the magnetism. High-resolution transmission electron microscopy (HRTEM) and scanning transmission electron microscopy (STEM) characterization show no nanoscale chemical inhomogeneities. Further experimental study may involve even more local probes, presumably at the single atom level, of the structure in the solid solution. Also of interest would be high resolution neutron diffraction studies to best quantify the positions of the oxygen atoms within the unit cells. We intentionally do not over-interpret the data obtained, but rather provide it as a basis for future experimental and theoretical study. In spite of the local monoclinic symmetry, the scaling of the magnetic properties with the long range structural characteristics suggests that for this system, modeling the electronic properties assuming the orthorhombic long range structures is best.

Acknowledgments

This research was supported by the Gordon and Betty Moore Foundation, grant GBMF-4412. The electron microscopy work was carried out at Brookhaven National Laboratory (BNL) and sponsored by the US Department of Energy (DOE) basic Energy Sciences (BES), by the Materials Sciences and Engineering Division under Contract DE-SC0012704. This research used resources of the National Synchrotron Light Source II, a U.S. Department of Energy (DOE) Office of Science User Facility operated for the DOE Office of Science by Brookhaven National Laboratory under Contract No. DE-SC0012704. Use of the Advanced Photon Source at Argonne National Laboratory was supported by the U. S. Department of Energy, Office of Science, Office of Basic Energy Sciences, under Contract No. DE-AC02-06CH11357. R.C. acknowledges inspiring discussions of this system with theorists Antoine Georges and Andrew Millis. The authors acknowledge Gihan Kwon for help with the PDF measurements and Daniel B. Straus for useful discussions of perovskite octahedral tilts.

References

- [1] Y. Maeno, S. Kittaka, T. Nomura, S. Yonezawa, and K. Ishida, *Journal of the Physical Society of Japan* 81, 011009 (2012).
- [2] J. Zheng, K. Ran, T. Li, J. Wang, P. Wang, B. Liu, Z.-X. Liu, B. Normand, J. Wen, and W. Yu, *Physical Review Letters* 119, (2017).
- [3] A. Banerjee, J. Yan, J. Knolle, C. A. Bridges, M. B. Stone, M. D. Lumsden, D. G. Mandrus, D. A. Tennant, R. Moessner, and S. E. Nagler, *Science* 356, 1055 (2017).
- [4] L. J. Sandilands, Y. Tian, K. W. Plumb, Y.-J. Kim, and K. S. Burch, *Physical Review Letters* 114, (2015).
- [5] K. Ran, J. Wang, W. Wang, Z.-Y. Dong, X. Ren, S. Bao, S. Li, Z. Ma, Y. Gan, Y. Zhang, J. T. Park, G. Deng, S. Danilkin, S.-L. Yu, J.-X. Li, and J. Wen, *Physical Review Letters* 118, (2017).
- [6] L. T. Nguyen, T. Halloran, W. Xie, T. Kong, C. L. Broholm, and R. J. Cava, *Physical Review Materials* 2, (2018).
- [7] I. Felner, I. Nowik, I. Bradaric, and M. Gospodinov, *Physical Review B* 62, 11332 (2000).
- [8] H. T. Dang, J. Mravlje, A. Georges, and A. J. Millis, *Physical Review B* 91, (2015).
- [9] J. S. Lee, Y. S. Lee, T. W. Noh, K. Char, J. Park, S.-J. Oh, J.-H. Park, C. B. Eom, T. Takeda, and R. Kanno, *Physical Review B* 64, (2001).
- [10] S. C. Gausepohl, M. Lee, R. A. Rao, and C. B. Eom, *Physical Review B* 54, 8996 (1996).
- [11] C. B. Eom, R. J. Cava, R. M. Fleming, J. M. Phillips, R. B. Vandover, J. H. Marshall, J. W. P. Hsu, J. J. Krajewski, and W. F. Peck, *Science* 258, 1766 (1992).
- [12] G. Koster, L. Klein, W. Siemons, G. Rijnders, J. S. Dodge, C.-B. Eom, D. H. A. Blank, and M. R. Beasley, *Reviews of Modern Physics* 84, 253 (2012).
- [13] J. M. Longo, P. M. Raccah, and J. B. Goodenough, *Journal of Applied Physics* 39, 1327 (1968).
- [14] M. Shepard, S. McCall, G. Cao, and J. E. Crow, *Journal of Applied Physics* 81, 4978 (1997).
- [15] R. S. Singh and K. Maiti, *Physical Review B* 76, (2007).
- [16] J.-G. Cheng, J.-S. Zhou, and J. B. Goodenough, *Proceedings of the National Academy of Sciences* 110, 13312 (2013).
- [17] Y. L. Wang, M. F. Liu, R. Liu, Y. L. Xie, X. Li, Z. B. Yan, and J.-M. Liu, *Scientific Reports* 6, (2016).
- [18] S. Middey, P. Mahadevan, and D. D. Sarma, *Physical Review B* 83, (2011).
- [19] J. B. Goodenough, *Czechoslovak Journal of Physics* 17, 304 (1967).
- [20] I. I. Mazin and D. J. Singh, *Physical Review B* 73, (2006).
- [21] S. Middey, P. Mahadevan, D. D. Sarma, A. Ghoshray, and B. Bandyopadhyay, *AIP Conference Proceedings* (2008).
- [22] L. Klein, L. Antognazza, T. H. Geballe, M. R. Beasley, and A. Kapitulnik, *Physical Review B* 60, 1448 (1999).
- [23] Y. S. Lee, J. Yu, J. S. Lee, T. W. Noh, T.-H. Gimm, H.-Y. Choi, and C. B. Eom, *Physical Review B* 66, (2002).
- [24] T. He and R. J. Cava, *Physical Review B* 63, (2001).
- [25] Cao, G., Korneta, O., Chikara, S., DeLong, L. E., & Schlottmann, P. arXiv preprint arXiv:0805.0741.
- [26] J. Gunasekera, L. Harriger, T. Heitmann, A. Dahal, H. Knoll, and D. K. Singh, *Physical*

- Review B 91, (2015).
- [27] L. Demkó, S. Bordács, T. Vojta, D. Nozadze, F. Hrahsheh, C. Svoboda, B. Dóra, H. Yamada, M. Kawasaki, Y. Tokura, and I. Kézsmárki, *Physical Review Letters* 108, (2012).
- [28] H. Kobayashi, M. Nagata, R. Kanno, and Y. Kawamoto, *Materials Research Bulletin* 29, 1271 (1994).
- [29] G. Cao, S. Mccall, M. Shepard, J. E. Crow, and R. P. Guertin, *Physical Review B* 56, 321 (1997).
- [30] F. Fukunaga and N. Tsuda, *Journal of the Physical Society of Japan* 63, 3798 (1994).
- [31] A. Kanbayasi, *Journal of the Physical Society of Japan* 44, 108 (1978).
- [32] I. Felner and U. Asaf, *Physica B: Condensed Matter* 337, 310 (2003).
- [33] Zarzycki, A., Rams, M., Goerlich, E. A., & Tomala, K. (2018). arXiv preprint arXiv:1806.03923.
- [34] B. H. Toby, *Journal of Applied Crystallography* 34, 210 (2001).
- [35] K. Momma and F. Izumi, *Journal of Applied Crystallography* 44, 1272 (2011).
- [36] C. L. Farrow, P. Juhas, J. W. Liu, D. Bryndin, E. S. Božin, J. Bloch, T. Proffen, and S. J. L. Billinge, *Journal of Physics: Condensed Matter* 19, 335219 (2007).
- [37] C. W. Jones, P. D. Battle, P. Lightfoot, and W. T. A. Harrison, *ChemInform* 20, (1989).
- [38] C. J. Howard and H. T. Stokes, *Acta Crystallographica Section B Structural Science* 54, 782 (1998).
- [39] R. H. Mitchell, *Perovskites: Modern and Ancient* (Almaz Press, Ontario, 2003).
- [40] N. Ross and R. Hazen, *Physics and Chemistry of Minerals* 17, (1990).
- [41] R. D. Shannon, *Acta Crystallographica Section A* 32, 751 (1976).
- [42] V. Petkov, I.-K. Jeong, J. S. Chung, M. F. Thorpe, S. Kycia, and S. J. L. Billinge, *Physical Review Letters* 83, 4089 (1999).
- [43] T. Proffen, *Zeitschrift Für Kristallographie - Crystalline Materials* 215, (2000).
- [44] J. Tao, D. Niebieskikwiat, M. B. Salamon, and J. M. Zuo, *Physical Review Letters* 94, (2005).
- [45] G. Cao, S. Chikara, X. N. Lin, E. Elhami, V. Durairaj, and P. Schlottmann, *Physical Review B* 71, (2005)
- [46] M. Shepard, G. Cao, S. Mccall, F. Freibert, and J. E. Crow, *Journal of Applied Physics* 79, 4821 (1996).
- [47] J. Okamoto, T. Okane, Y. Saitoh, K. Terai, S.-I. Fujimori, Y. Muramatsu, K. Yoshii, K. Mamiya, T. Koide, A. Fujimori, Z. Fang, Y. Takeda, and M. Takano, *Physical Review B* 76, (2007).
- [48] B. Lin, C. Lin, Y. Wu, and H. Ku, *Journal of Magnetism and Magnetic Materials* 272-276, 479 (2004).
- [49] H.-T. Jeng, S.-H. Lin, and C.-S. Hsue, *Physical Review Letters* 97, (2006).
- [50] J. J. Hamlin, S. Deemyad, J. S. Schilling, M. K. Jacobsen, R. S. Kumar, A. L. Cornelius, G. Cao, and J. J. Neumeier, *Physical Review B* 76, (2007).
- [51] See Supplemental Material at URL for Long-range and local crystal structures of the $\text{Sr}_{1-x}\text{Ca}_x\text{RuO}_3$ Perovskites.

Table 1: Lattice parameters, average bond lengths and bond angles in $\text{Sr}_{1-x}\text{Ca}_x\text{RuO}_3$ system calculated from the GSAS refinement of x-ray synchrotron powder diffraction data.

x in $\text{Sr}_{1-x}\text{Ca}_x\text{RuO}_3$	Lattice parameter (Å)	Average Ru-O axial (Å)	Average Ru-O equatorial (Å)	Average (Sr/Ca)-O (Å)	Average O-Ru-O (°)	χ^2
0	a = 5.532338(6) b = 7.848885(9) c = 5.571862(5)	1.988(3)	1.9842(5)	2.6774	89.38	1.063
0.1	a = 5.53048(2) b = 7.84090(4) c = 5.56060(2)	1.995(3)	1.9918(8)	2.6685	89.45	1.159
0.2	a = 5.5261(3) b = 7.8254(4) c = 5.5416(3)	1.991(3)	1.9767(1)	2.6559	89.578	1.962
0.3	a = 5.52210(2) b = 7.80917(3) c = 5.52947(2)	2.015(4)	1.9766(7)	2.6435	88.398	1.750
0.4	a = 5.51546(3) b = 7.79265(8) c = 5.50844(5)	1.983(4)	1.9827(2)	2.6094	89.458	1.510
0.5	a = 5.51462(3) b = 7.77921(5) c = 5.49551(3)	1.993(3)	2.0080(3)	2.5876	88.03	1.684
0.6	a = 5.51913(4) b = 7.78035(8) c = 5.48708(5)	1.969(3)	2.0031(2)	2.5649	88.81	3.478
0.7	a = 5.52077(4) b = 7.74664(5) c = 5.45000(4)	1.994(0)	1.9779(2)	2.5551	88.71	1.409
0.8	a = 5.52328(3) b = 7.71384(4) c = 5.41858(3)	1.998(3)	1.9874(7)	2.5388	89.41	1.744
0.9	a = 5.52767(3) b = 7.68729(4) c = 5.38824(3)	2.002(3)	1.9821(8)	2.5138	89.05	3.420
1	a = 5.534338(7) b = 7.662086(9) c = 5.356035(7)	1.997(2)	1.9845(6)	2.4927	89.28	1.876

Table 2: Atomic parameters for both orthorhombic ($Pnma$) and monoclinic ($P2_1/m$) structures of $SrRuO_3$ and $CaRuO_3$ by PDF analysis for atomic separations between 1.5 and 5 angstroms.

$SrRuO_3$ -Orthorhombic average structure - space group $Pnma$ (No. 62). $A = 5.5405(7)$ Å, $b = 7.8425(4)$ Å, $c = 5.5804(2)$ Å, $\alpha = \beta = \gamma = 90^\circ$.

Atom	Wyckoff.	Occ.	x	y	z	U_{iso}
Sr	4c	1	0.01647(2)	¼	0.99522(6)	0.0057(4)
Ru1	4b	1	0	0	½	0.0028(6)
O1	8d	1	0.27292(7)	0.02941(9)	0.71061(0)	0.0139(9)
O2	4c	1	0.55359(2)	¼	0.07532(9)	0.0139(9)

$CaRuO_3$ -Orthorhombic average structure - space group $Pnma$ (No. 62). $a = 5.5641(0)$ Å, $b = 7.6051(3)$ Å, $c = 5.3689(5)$ Å, $\alpha = \beta = \gamma = 90^\circ$.

Atom	Wyckoff.	Occ.	x	y	z	U_{iso}
Ca	4c	1	0.05639(6)	¼	0.98534(2)	0.0010(4)
Ru1	4b	1	0	0	½	0.00028(4)
O1	8d	1	0.29027(2)	0.05194(7)	0.69840(3)	0.0015(2)
O2	4c	1	0.45932(2)	¼	0.08989(9)	0.0015(2)

$SrRuO_3$ -Monoclinic local structure - space group $P2_1/m$ (No. 11), unique axis b . $a = 5.5445(6)$ Å, $b = 7.8453(9)$ Å, $c = 5.5825(1)$ Å, $\alpha = 90^\circ$, $\beta = 91.08(8)^\circ$, $\gamma = 90^\circ$.

Atom	Wyckoff.	Occ.	x	y	z	U_{iso}
Sr1	2e	1	0.01778(1)	¼	0.99479(0)	0.00349(4)
Sr2	2e	1	0.51872(0)	¼	0.50476(5)	0.00360(0)
Ru1	2b	1	½	0	0	0.00184(7)
Ru2	2c	1	0	0	½	0.00186(8)
O1	4f	1	0.27015(9)	0.02989(2)	0.72236(1)	0.01053(4)
O2	4f	1	0.22179(2)	0.96011(6)	0.21718(3)	0.00936(5)
O3	2e	1	0.46057(7)	¼	0.05751(6)	0.02675(5)
O4	2e	1	0.93558(7)	¼	0.44432(7)	0.02227(4)

$CaRuO_3$ -Monoclinic local structure - space group $P2_1/m$ (No. 11), unique axis b . $a = 5.5854(9)$ Å, $b = 7.6466(7)$ Å, $c = 5.3284(1)$ Å, $\alpha = 90^\circ$, $\beta = 91.41(4)^\circ$, $\gamma = 90^\circ$.

Atom	Wyckoff.	Occ.	x	y	z	U_{iso}
Ca1	2e	1	0.56900(1)	¼	0.50037(6)	0.00465(1)
Ca2	2e	1	0.04472(9)	¼	0.97380(0)	0.00419(8)
Ru1	2b	1	½	0	0	0.00182(4)
Ru2	2c	1	0	0	½	0.00188(9)
O1	4f	1	0.76069(5)	0.05181(6)	0.80755(1)	0.00258(1)
O2	4f	1	0.30343(1)	0.45231(9)	0.68332(9)	0.00131(0)
O3	2e	1	0.95290(2)	¼	0.41495(4)	0.00153(6)
O4	2e	1	0.45091(1)	¼	0.11188(9)	0.00227(2)

Figure Captions

Figure 1: The pseudo-cubic perovskite subcells. The lattice parameters b and c (b divided by 2 and c divided by square root of 2 to normalize them to a standard perovskite subcell) decrease in the perovskite solid solution on going from SrRuO_3 to CaRuO_3 , while the normalized lattice parameter a (normalized in the same fashion as c is normalized) remains relatively constant with a minimum at around $x = 0.4$. Near this composition the material is dimensionally nearly cubic ($a/(\text{sqrt } 2)$ and $c/(\text{sqrt } 2) \approx b/2$). The standard deviations are smaller than the plotted points in all panels. Inset: The perovskite subcells for SrRuO_3 and CaRuO_3 (RuO_6 octahedra rendered, oxygens shown at the vertices, Sr and Ca balls in the cavities.) The lines are guides to the eye.

Fig. 2: The composition dependence of the perovskite cell and cavity volumes. Specification of the (a) cell volume and (b) A-site cavity volume as a function of composition in the $\text{Sr}_{1-x}\text{Ca}_x\text{RuO}_3$ solid solution and (c) their ratio. The lines are guides to the eye.

Figure 3: The perovskite tilt angles determined from the average structures (a) The [001], [110] and [111] perovskite tilt angles (taken as the deviation from the ideal 180 degree Ru-O-Ru bond angle) for compounds in the $\text{Sr}_{1-x}\text{Ca}_x\text{RuO}_3$ solid solution. (b) The average perovskite tilt angle as a function of composition. The average tilt is obtained by averaging over the [001] [110] and [111] directions. The lines are guides to the eye.

Figure 4: Further characterization of the crystal structures (a) The average tilt of the RuO_6 octahedra in the $\text{Sr}_{1-x}\text{Ca}_x\text{RuO}_3$ perovskites plotted as function of the observed tolerance factor. Inset shows the variation with “theoretical” tolerance factor, and (b) the variance of the A-O bond lengths ($A = \text{Sr}/\text{Ca}$) as a function of perovskite tilt.

Figure 5: The X-ray PDF data for SrRuO_3 and CaRuO_3 for the “average structure” 15-30 angstrom atomic separation range. Black dots are the data for $G(r)$ and the red lines are the resulting values for $G(r)$ obtained from the synchrotron powder diffraction data structural refinements. The fits are excellent and indicate that the long-range structures of SrRuO_3 and CaRuO_3 found in the PDF experiments agree well with the average structure determined through the synchrotron diffraction data refinements.

Figure 6: PDF-based local structure comparison of orthorhombic ($Pnma$) and monoclinic ($P2_1/m$) models for CaRuO_3 and SrRuO_3 . The PDF data for $G(r)$ are the open circles while the fits are shown as red lines. The fits to the locally monoclinic structures ((c) and (d)) are better than the fits to the orthorhombic models obtained from the long range (average) structure refinements. Although CaRuO_3 is fit very well, minor discrepancies surprisingly remain for SrRuO_3 .

Figure 7: Transmission Electron Microscope Characterization at the nanoscale. Left panel: (a) An electron diffraction pattern of $\text{Sr}_{0.7}\text{Ca}_{0.3}\text{RuO}_3$ in the [010] zone, obtained from an area about 150 nm in diameter. (b) A typical EDX spectrum of $\text{Sr}_{0.7}\text{Ca}_{0.3}\text{RuO}_3$. (c) A HRTEM image and (d) a HAADF-STEM image of $\text{Sr}_{0.7}\text{Ca}_{0.3}\text{RuO}_3$ (in the [010] zone). Right panel: (e-h) Similar measurements on $\text{Sr}_{0.5}\text{Ca}_{0.5}\text{RuO}_3$. Defects can be seen in the crystal structure in the (g) HRTEM image. (h) The AHAADF-STEM image shows the typical atomic arrangements in the a - b plane in areas without defects, in addition to the extended defects.

Figure 8: The magnetic characterization of the perovskites in the $\text{Sr}_{1-x}\text{Ca}_x\text{RuO}_3$ system. (a) Magnetic susceptibility, (b) its inverse as function of temperature.

Figure 9: Composition dependence of the magnetic properties. (a) The difference between the observed magnetic susceptibility at 300 K and temperature-independent susceptibility. (b) Effective moment and (c) Curie-Weiss temperature as functions of x in the $\text{Sr}_{1-x}\text{Ca}_x\text{RuO}_3$ perovskites. A comparison between our work (solid symbols) and prior studies Ref. 29 (orange squares) and Ref. 30 (blue circles) is shown. The lines are guides to the eye.

Figure 10: The Curie-Weiss temperature and temperature of transition to the ferromagnetic state in $\text{Sr}_{1-x}\text{Ca}_x\text{RuO}_3$ (a) as a function of perovskite tilt angle and (b) as a function of the unit cell volume. Shown for comparison in panel (b) is the data for the change in the ferromagnetic T_c of SrRuO_3 under applied pressure, taken from reference 49. The lines are guides to the eye.

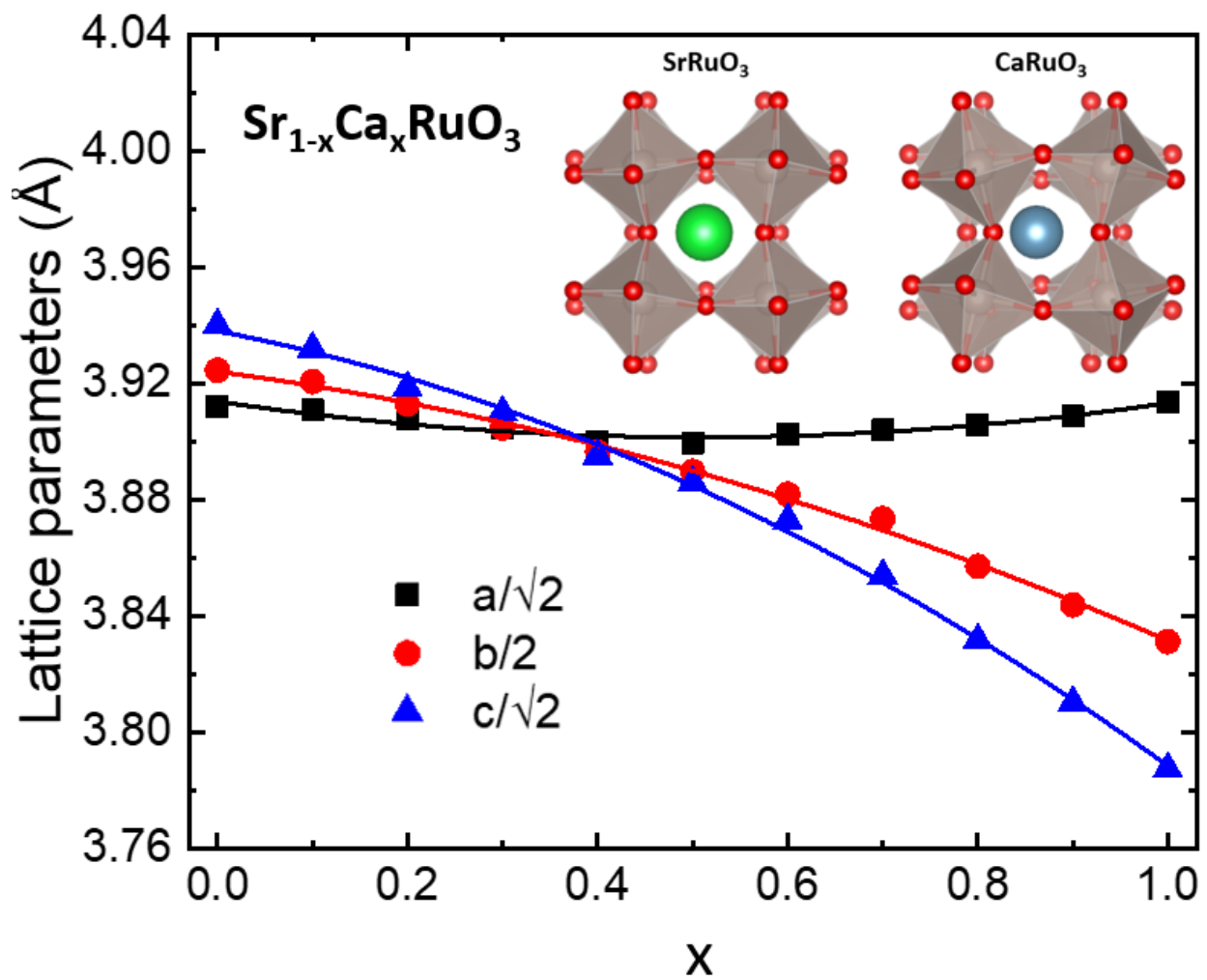


Fig. 1

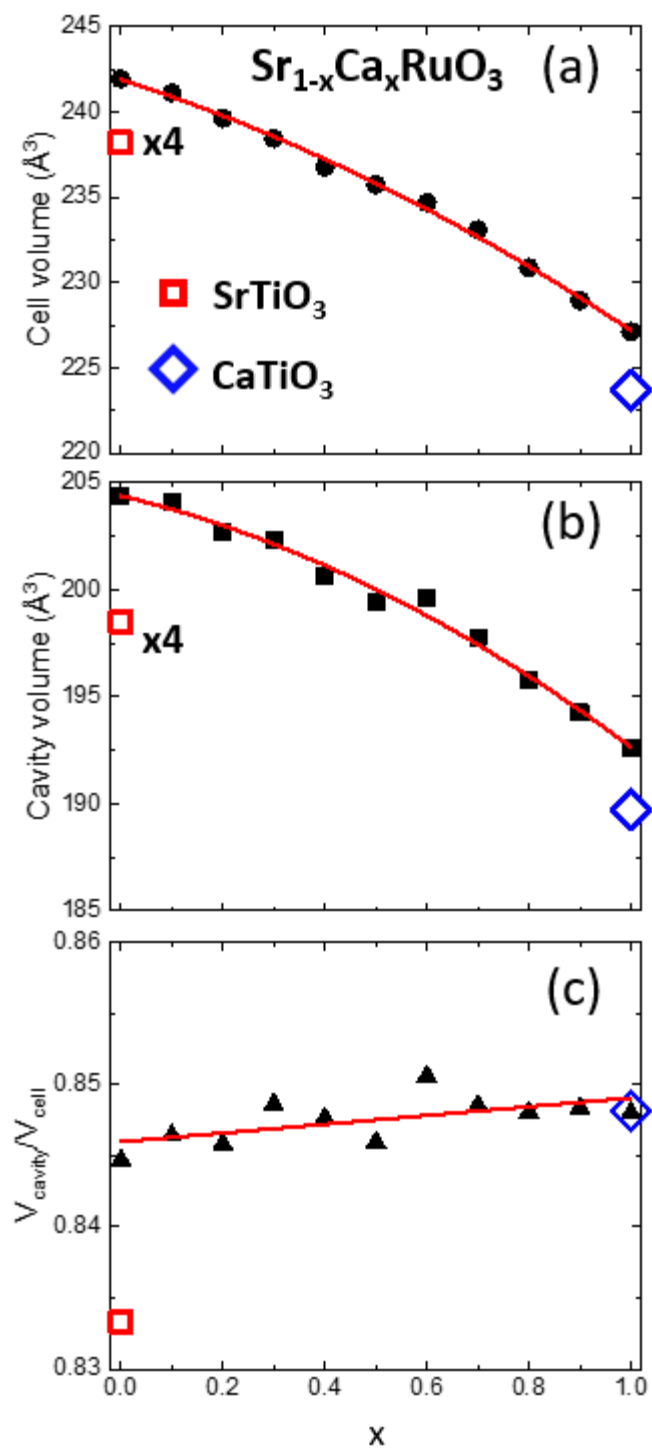


Fig. 2

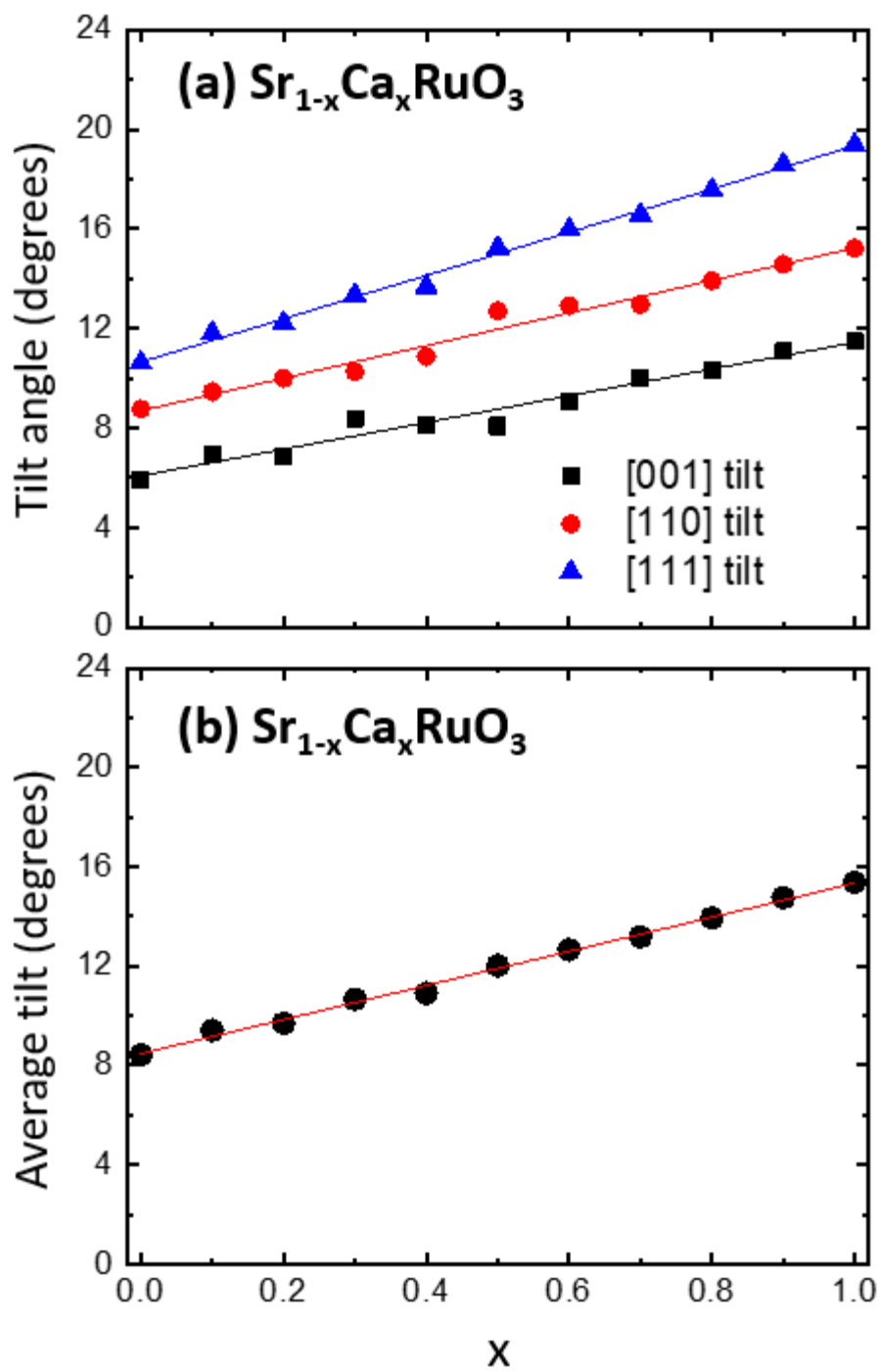


Fig. 3

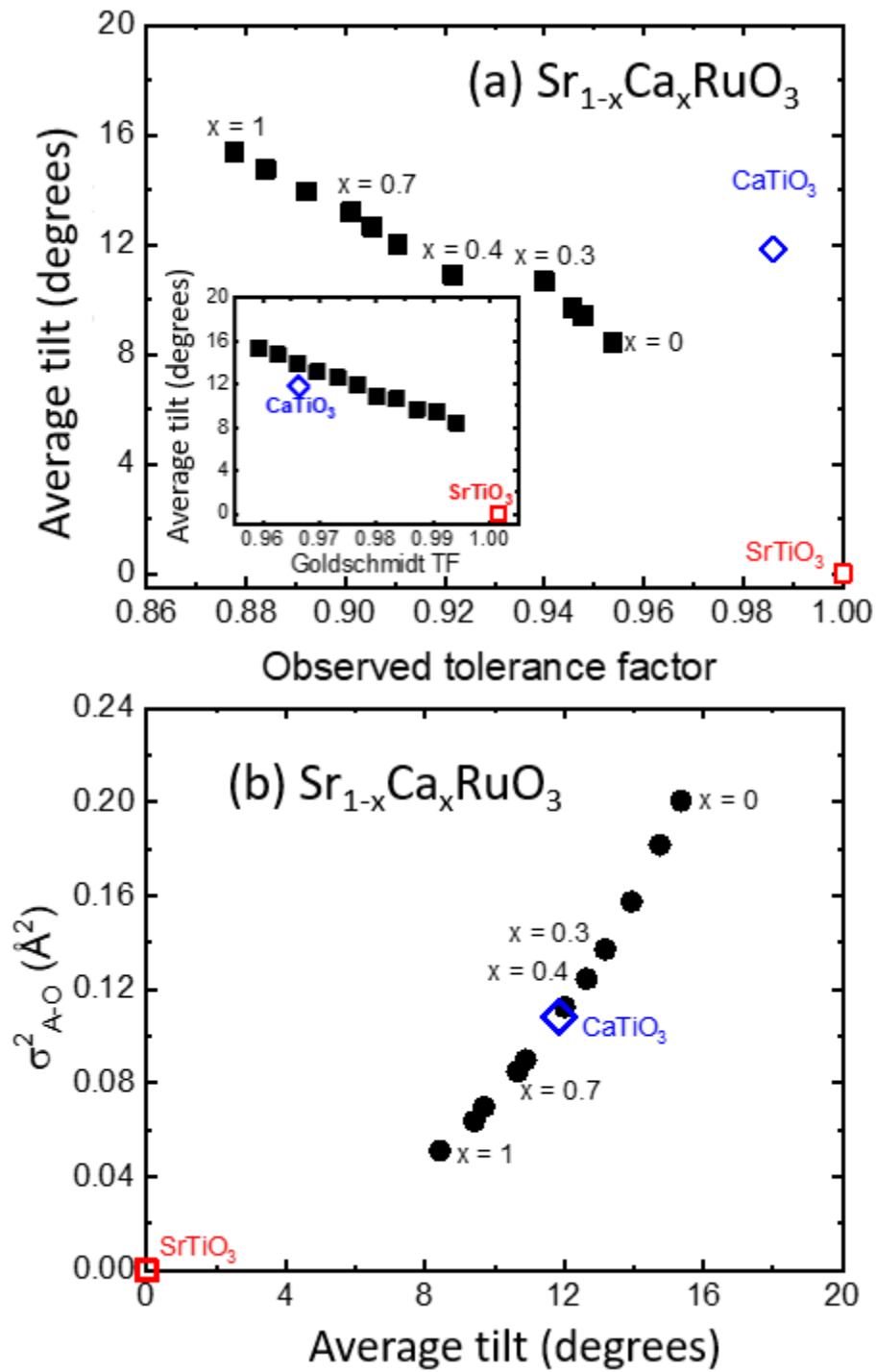


Fig. 4

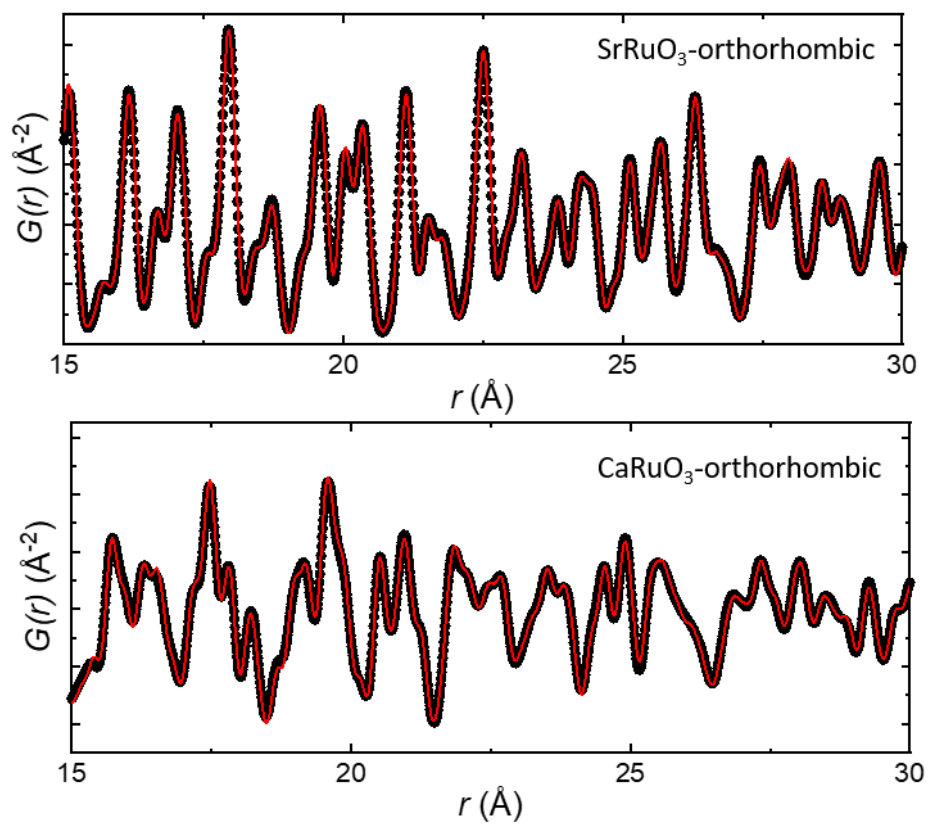


Fig. 5

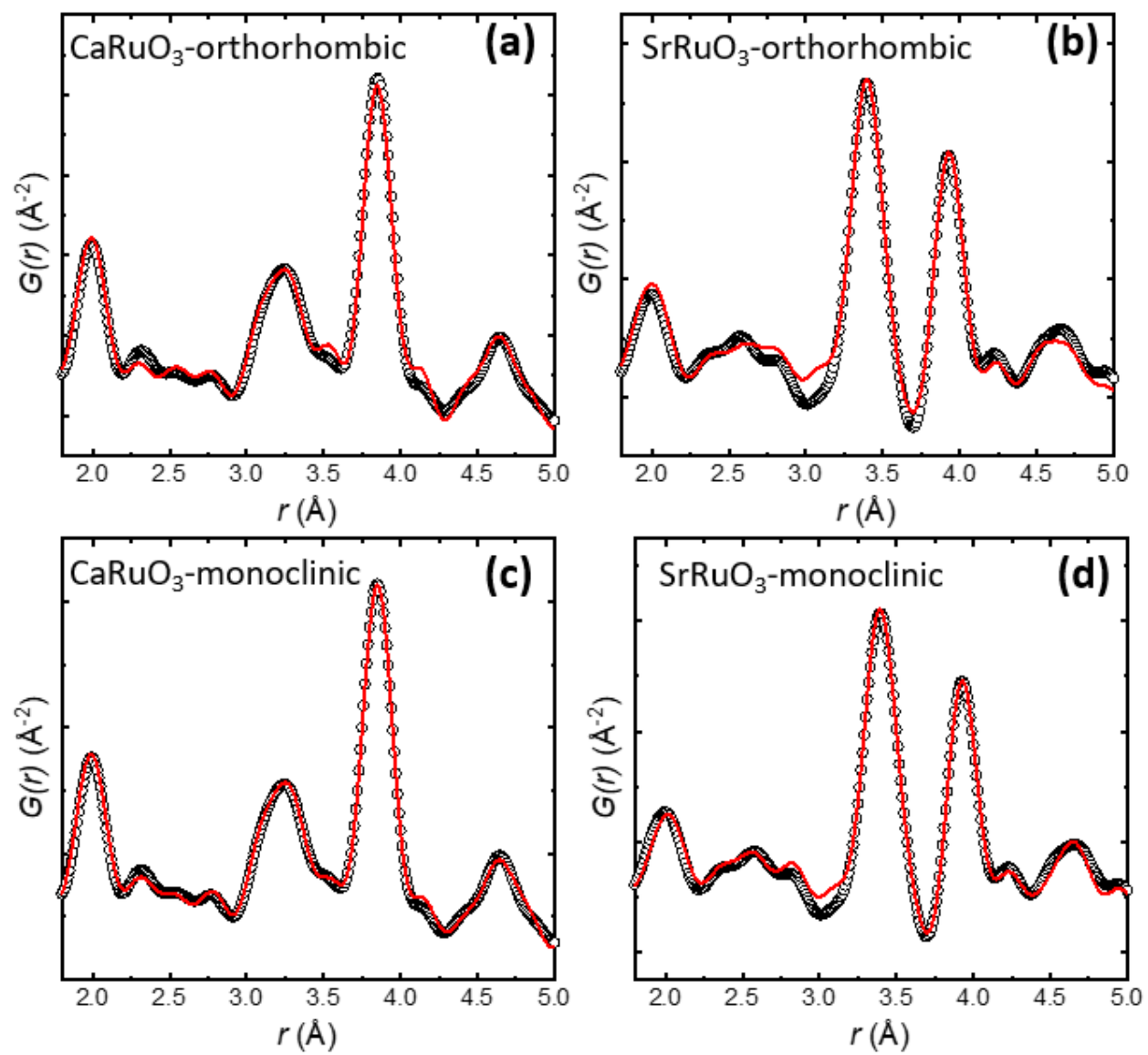


Fig. 6

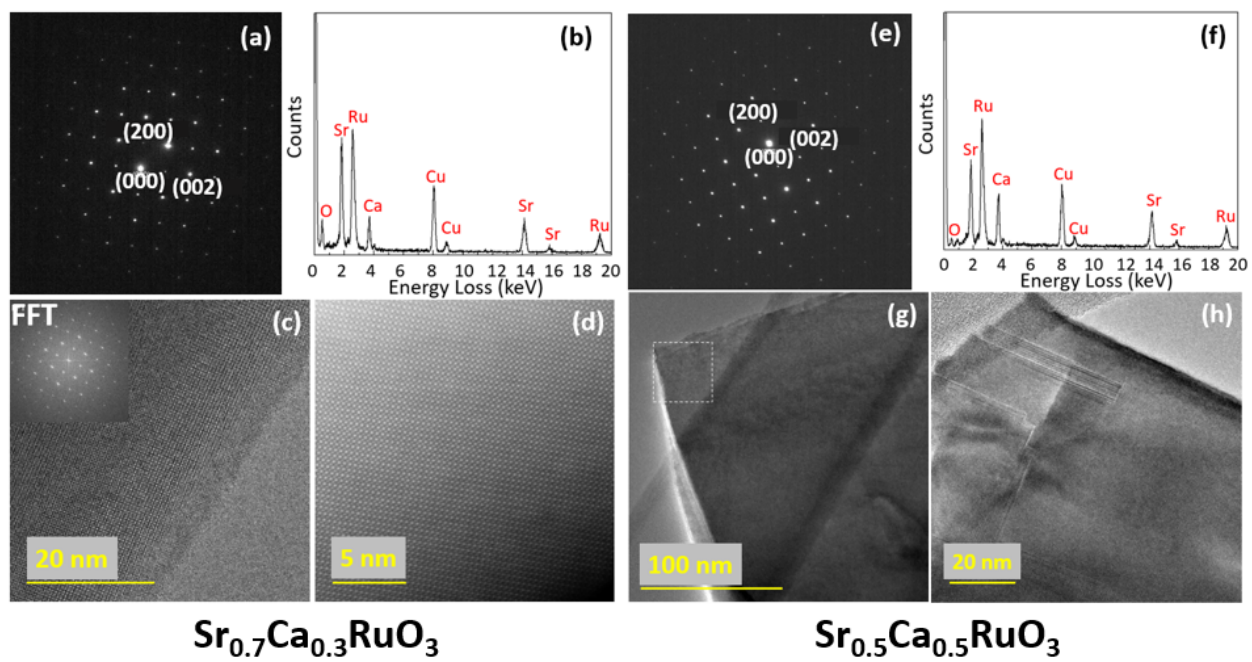


Fig. 7

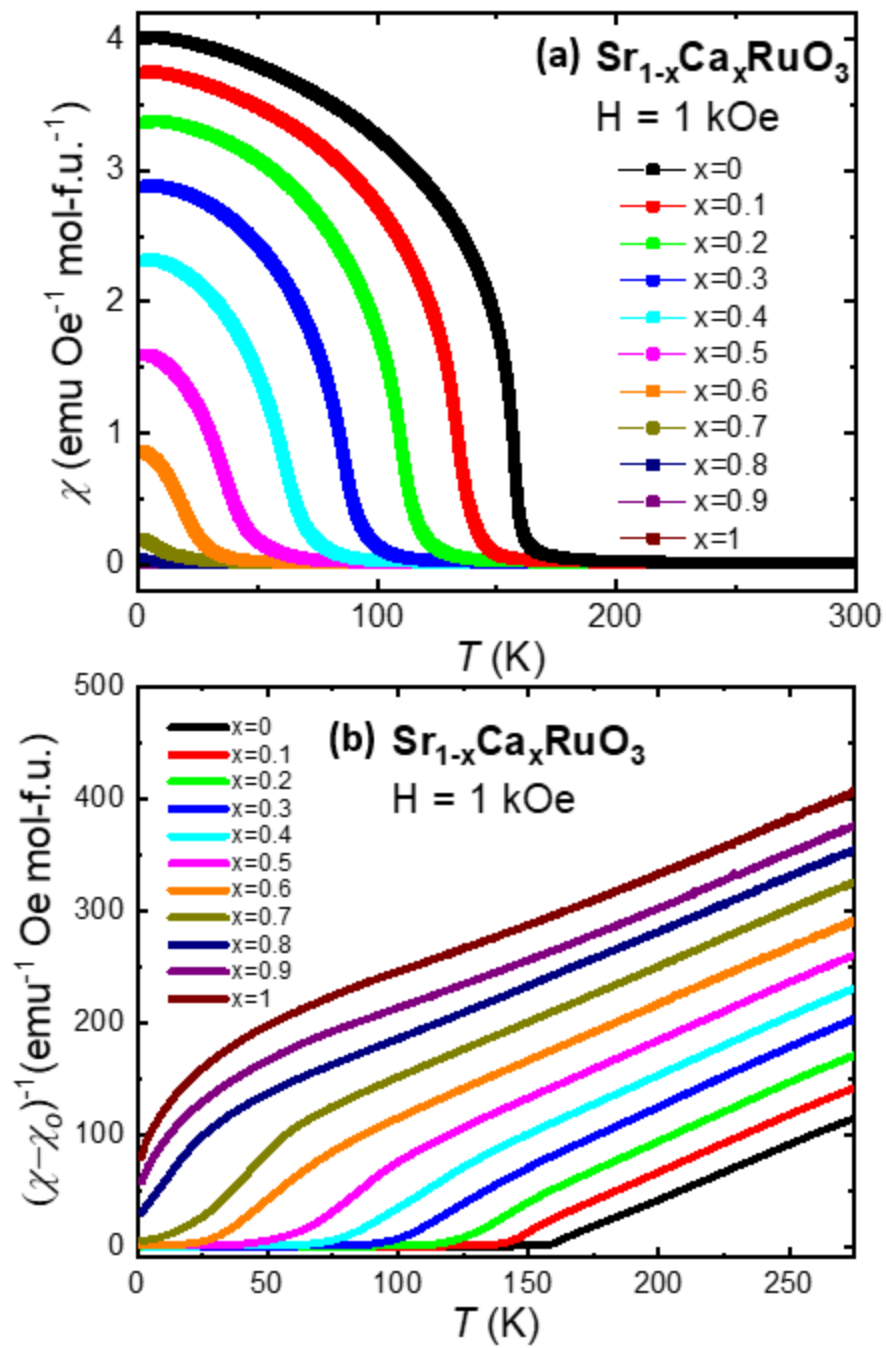


Fig. 8

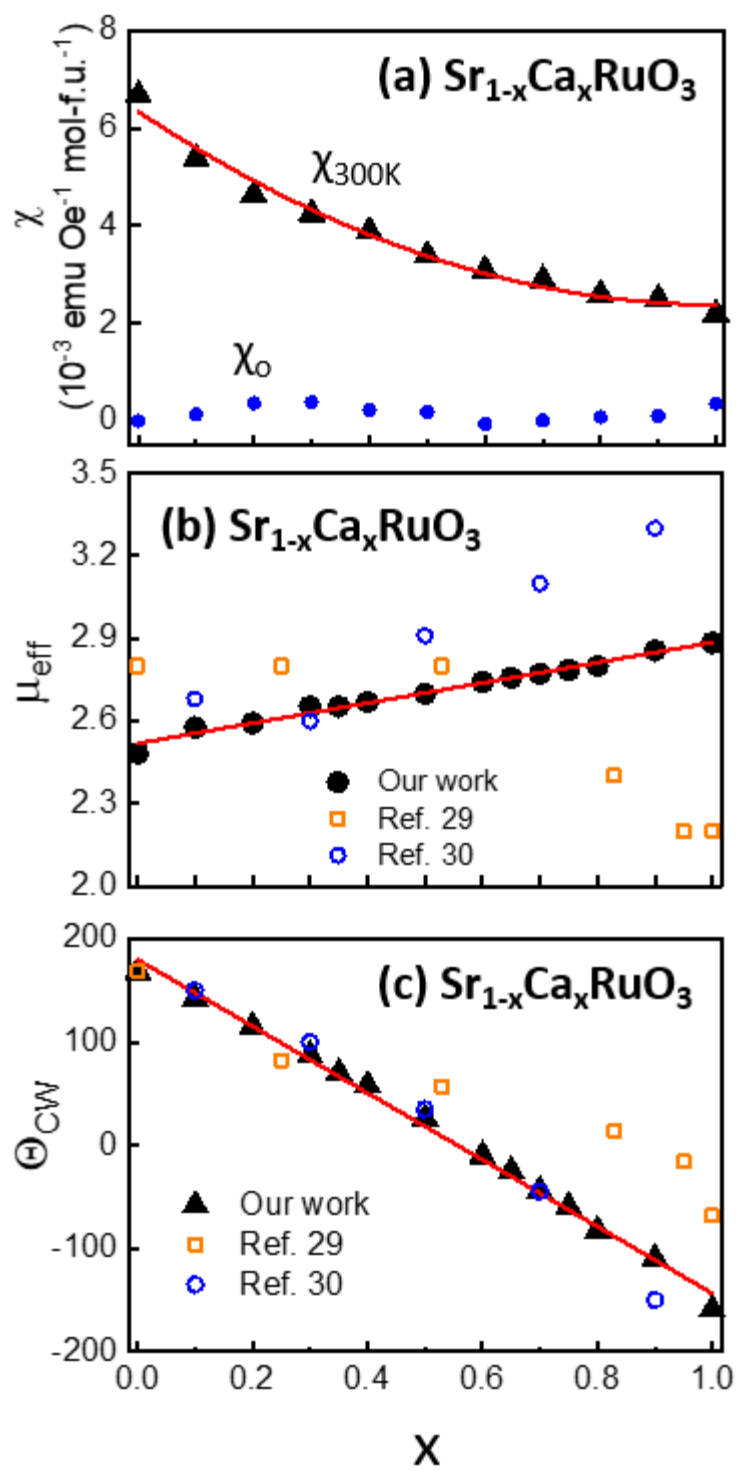


Fig. 9

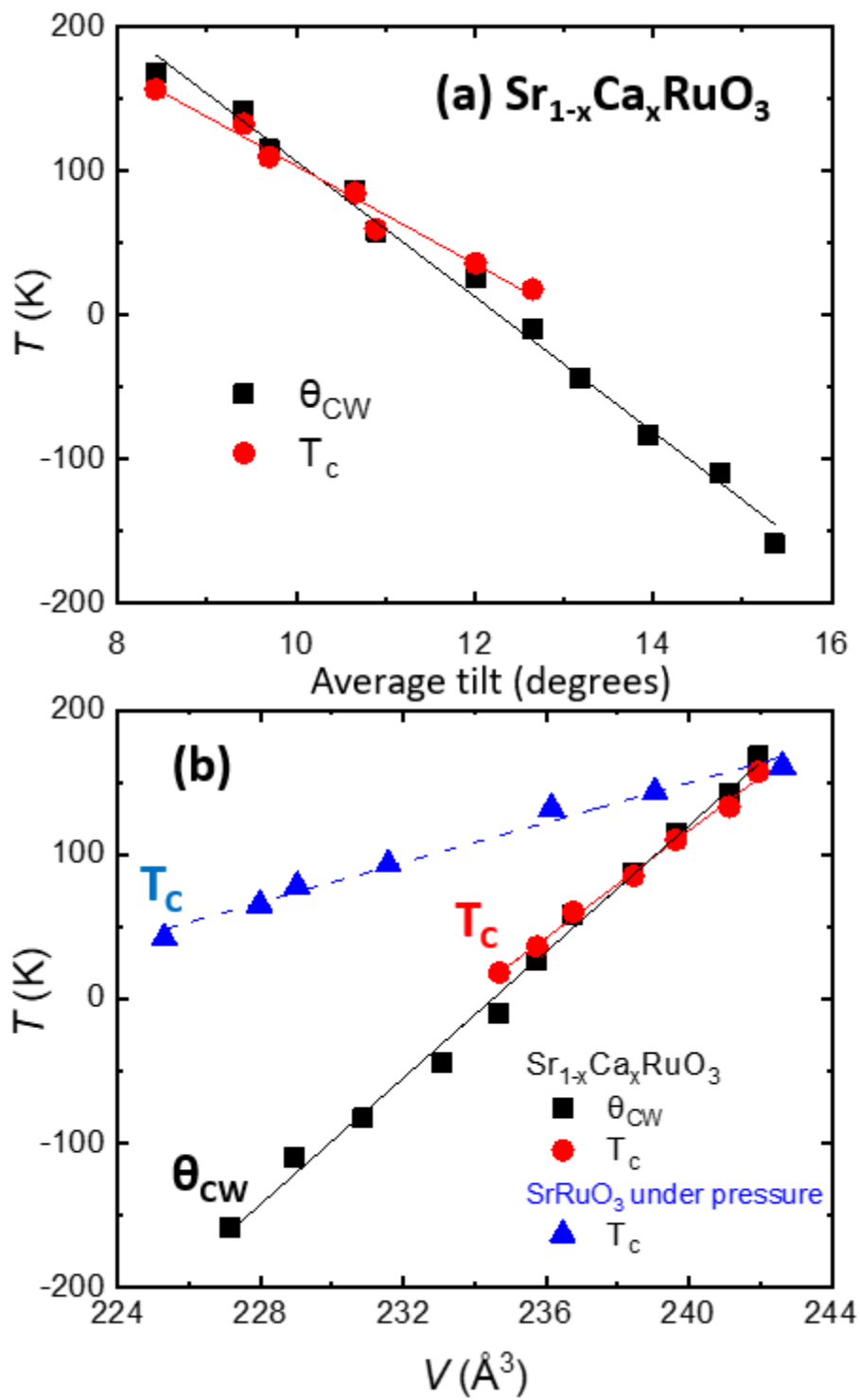


Fig. 10